


RESEARCH ARTICLE | JULY 12 2023

# Heat transfer in porous media Rayleigh–Bénard convection at various Prandtl numbers

Special Collection: [Turbulence in Plasmas and Fluids](#)

Zang Xuehao (臧学昊) ; Zhong Jun (钟俊)  ; Sun Chao (孙超) 

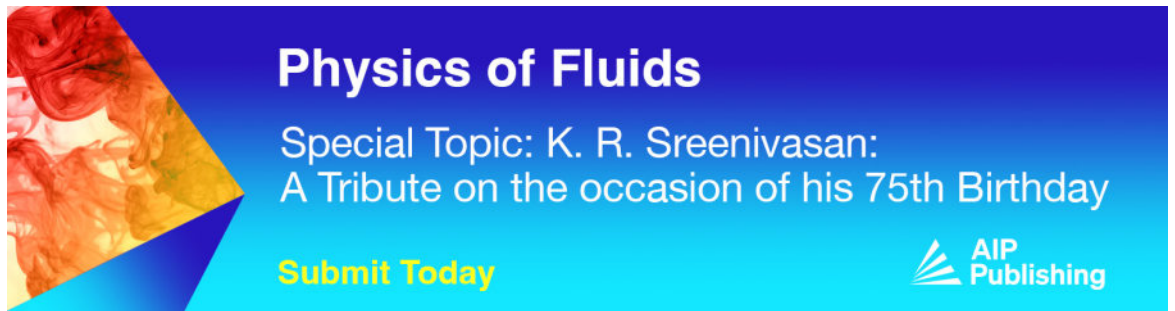
 Check for updates

*Physics of Fluids* 35, 075124 (2023)

<https://doi.org/10.1063/5.0157666>




CrossMark



**Physics of Fluids**  
Special Topic: K. R. Sreenivasan:  
A Tribute on the occasion of his 75th Birthday

[Submit Today](#)



# Heat transfer in porous media Rayleigh–Bénard convection at various Prandtl numbers

Cite as: Phys. Fluids **35**, 075124 (2023); doi: 10.1063/5.0157666

Submitted: 9 May 2023 · Accepted: 27 June 2023 ·

Published Online: 12 July 2023



View Online



Export Citation



CrossMark

Xuehao Zang (臧学昊),<sup>1,2</sup> Jun Zhong (钟俊),<sup>1,a)</sup> and Chao Sun (孙超)<sup>1,3</sup>

## AFFILIATIONS

<sup>1</sup>Center for Combustion Energy, Key Laboratory for Thermal Science and Power Engineering of Ministry of Education, and Department of Energy and Power Engineering, Tsinghua University, 100084 Beijing, China

<sup>2</sup>Weiyang College, Tsinghua University, 100084 Beijing, China

<sup>3</sup>Department of Engineering Mechanics, School of Aerospace Engineering, Tsinghua University, 100084 Beijing, China

**Note:** This paper is part of the special topic, Turbulence in Plasmas and Fluids.

**a)** Author to whom correspondence should be addressed: zhong-j21@mails.tsinghua.edu.cn

## ABSTRACT

We perform two-dimensional direct numerical simulations to study the effect of porous media on global transport properties and flow structures in Rayleigh–Bénard (RB) convection at different Prandtl numbers. The simulations are carried out in a square RB cell with uniformly placed circular obstacles, where the porosity spans between  $\phi = 1$  and  $\phi = 0.75$  with the Rayleigh number  $Ra$  fixed at  $10^8$ , at two high Prandtl numbers (10, 4.3) and two low Prandtl numbers (0.03, 0.1). It is found that the Nusselt number  $Nu$  varies non-monotonically with decreasing porosity, first increased and then suppressed at both high- $Pr$  and low- $Pr$  cases, while the transition points are greatly advanced at low  $Pr$ . Though the trends are similar at low and high  $Pr$ , we point out that the physical mechanisms behind them are different. At high  $Pr$ , the porous media enhance the heat transfer by increasing the flow coherence at high porosity and inhibit the heat transfer by impeding the passage of the plume in the bulk region at low porosity. However, at low  $Pr$ , the viscous effect is weakened and the heat transfer is mainly through the large-scale circulation (LSC). As the porosity decreases, the LSC is enhanced and the flow is laminarized, inhibiting the shedding of the plume from the boundary layer. Moreover, we further explore the flow structure under the random distribution of obstacles and find some similarities in the evolution of the flow structure. The discovery of the new mechanism for porous media at low  $Pr$  advances the understanding of the effect of porous media on natural convection and may provide implications for industrial designs.

Published under an exclusive license by AIP Publishing. <https://doi.org/10.1063/5.0157666>

## I. INTRODUCTION

Thermal convection is a ubiquitous phenomenon in nature and industrial technology.<sup>1–4</sup> Rayleigh–Bénard (RB) convection, the buoyancy-driven flow of a fluid layer heated from below and cooled from above, has been studied extensively as a paradigmatic system for decades.<sup>5–10</sup> Due to temperature difference, an uneven density profile occurs in the RB cell, and the resulting buoyancy drives the convection. In traditional RB convection, a large-scale circulation (LSC) is formed, and thermal plumes transfer heat from the bottom boundary layer to the top.<sup>5,11–14</sup> The controlling parameters governing the turbulent flow are the Rayleigh number (measuring the buoyancy-driving strength)  $Ra$  and the Prandtl number (fluid property)  $Pr$ , while the response parameters are the Nusselt number (measuring the heat transfer efficiency)  $Nu$  and the Reynolds number (measuring the flow strength)  $Re$ . The scaling law between the response parameters and the controlling

parameters has been one of the central research issues and has obtained the attention of many researchers.<sup>1,2,15–17</sup>

Additionally, other physical effects are introduced to modulate the transport efficiency of RB convection, such as applying wall shear,<sup>18,19</sup> rough surfaces,<sup>20,21</sup> geometrical confinement,<sup>22,23</sup> and horizontal vibration.<sup>24</sup> One related problem of RB convection in a fluid-saturated porous media has drawn increasing attention due to numerous industrial applications, including carbon dioxide sequestration and geothermal energy extraction.<sup>25–27</sup> In recent years, considerable progress has been made in theoretical, numerical, and experimental work to investigate how porous media affect flow structures and heat transfer properties.<sup>28–32</sup>

In the presence of porous media, the flow structure appears much more complicated. The flow in a porous media is subjected to driving buoyancy force and viscous drag from the porous matrix, quantified by the porosity  $\phi$ . The porous media can form some flow

channels due to boundary restrictions, which may enhance the global heat transport by increasing the coherence of the flow. In the numerical study, Liu *et al.*<sup>32</sup> added circular, solid obstacles on a square lattice and reported the non-monotonic behavior of  $Nu(\phi)$ . Under specific porosity, the LSC is significantly restrained, and thermal plumes through convective channels serve as primary heat carriers in the system. As  $\phi$  decreases from 1, heat transport is enhanced by the highly coherent thermal plumes, but eventually suppressed due to the weakening of flow motion. Relevant experiments have also confirmed these results.<sup>29</sup> Similar competing effects are also observed by Chong *et al.*<sup>6</sup> in confined RB convection, rotating RB convection, and double diffusive convection. In all of these cases, optimal heat transport was observed at moderate strength of stabilizing forces with  $Pr \geq 0.5$ .

In practical scenarios, fluids with different thermal properties are applied, and varying  $Pr$  may lead to drastic changes in heat transport processes. For instance, around room temperature of  $T = 25^\circ\text{C}$ , the Prandtl number is 6.90 for water, 0.72 for air, and 0.02 for mercury,<sup>33</sup> with a change of more than two orders of magnitude. As a result, the effect of  $Pr$  on the heat transport and flow structure in RB convection has also been discussed over the last decade. Yang *et al.*<sup>7</sup> found that the heat transfer enhancement shows a maximum as a function of  $Pr$  in rotating RB systems. Chong *et al.*<sup>23</sup> analyzed how  $Pr$  influences confinement-induced heat transport enhancement by modifying global flow structures. It is reported that for small  $Pr$ , the large-scale circulation is robust regardless of the width-to-height aspect of geometrical confinement.

Regarding porous media RB convection, however, the Prandtl number is usually fixed for simplification, and few investigations have focused on the low- $Pr$  heat transport process in porous media. As an important controlling parameter,  $Pr$  represents the ratio between viscous diffusivity and thermal diffusivity, affecting the resistance of the porous media to the fluid. At low  $Pr$ , the flow structure of the porous media RB convection may be quite different. Inspired by this, we perform a 2D pore-scaled direct numerical simulation with  $Pr$  ranging from 0.03 to 10, and circular solid obstacles with no-slip boundary conditions are included in an RB convection cell to model porous structures. We focus on the heat transfer efficiency and the flow structures and aim to investigate the effect of  $Pr$  on the porous media RB convection by comparing the high- $Pr$  and low- $Pr$  cases. Furthermore, our study attempts to provide a deeper insight into the coupling mechanism of porous structures and heat transport properties and shed light on applications in possible industrial scenarios.

The rest of the paper is organized as follows: In Sec. II, the governing equations, the numerical model, and the simulation parameters are described in detail. In Sec. III, we present our main results, focusing on the heat transfer properties, flow structures, and boundary layer properties. In Sec. IV, we additionally discuss the influence of different distributions of obstacles. The findings are summarized in Sec. V.

## II. NUMERICAL MODEL

In this study, we set up a two-dimensional square RB cell of length  $L$ , and the fluid inside is heated below and cooled above. To explore the detailed flow through porous structures, we model the porous media as shown in Fig. 1: Circular solid obstacles of diameter  $D$  are placed uniformly on an  $N$ -by- $N$  square lattice with spacing  $l$ . The porosity  $\phi$  is defined as the volume fraction of the fluid phase, and  $\phi = 1$  corresponds to the traditional RB convection with no

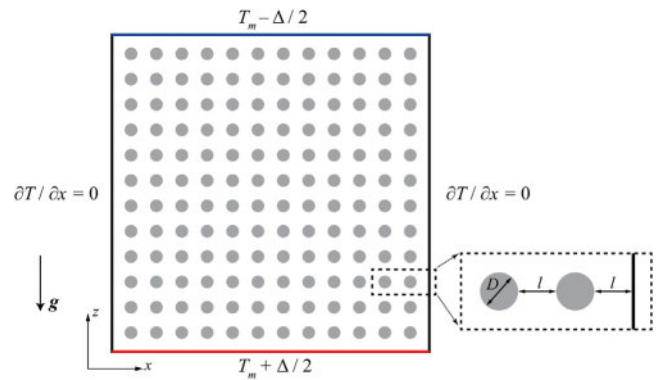


FIG. 1. Schematic diagram of the 2D RB convection in porous media.

obstacle. In this system with an unity aspect ratio, we have  $l = (L - ND)/(N + 1)$  and  $\phi = 1 - N^2\pi D^2/(4L^2)$ , where we choose  $D = 0.04L$  here.

The lower and upper plates satisfy isothermal conditions with the temperature difference  $\Delta$ , and the two side walls are set to adiabatic conditions. The obstacles are set to be thermally conductive with the same thermal properties as the fluid for simplification, which is based on our previous findings that the heat transfer efficiency and the flow structure of porous media RB system only weakly depend on the thermal conductivity of the porous material.<sup>34</sup> In addition, the no-slip and no-penetration conditions are applied for all cell boundaries and obstacle surfaces.

The dimensionless governing equations of the system with the Oberbeck–Boussinesq approximation, for the non-dimensional quantities including velocity  $\mathbf{u} = (u, v)$ , temperature  $T$ , and pressure  $p$ , read<sup>32</sup>

$$\begin{aligned} \nabla \cdot \mathbf{u} &= 0, \\ \frac{\partial \mathbf{u}}{\partial t} + \mathbf{u} \cdot \nabla \mathbf{u} &= -\nabla p + \sqrt{\frac{Pr}{Ra}} \nabla^2 \mathbf{u} + T \mathbf{e}_z + \mathbf{f}, \\ \frac{\partial T}{\partial t} + \nabla \cdot (\mathbf{u} T) &= \sqrt{\frac{1}{Ra \cdot Pr}} \nabla^2 T, \end{aligned} \quad (1)$$

where  $\mathbf{e}_z$  is the unit vector in the vertical direction, and  $\mathbf{f}$  is added as the resistance force of the obstacle array. We use scaled quantities including  $L$  for length,  $\Delta$  for temperature, the free fall velocity  $U = \sqrt{g\beta\Delta L}$  for velocity, and  $L/U$  for time to non-dimensionalize the equations, where  $g$  is the gravitational acceleration, and  $\beta$  is the coefficient of thermal expansion of the fluid.

For a fixed porous matrix, the two non-dimensional parameters, including the Rayleigh number  $Ra = g\beta\Delta L^3/(\nu\kappa)$  and the Prandtl number  $Pr = \nu/\kappa$ , control the convection system, where  $\nu$  is the kinematic viscosity, and  $\kappa$  is the thermal diffusivity of the fluid. The response parameters include the Nusselt number  $Nu = \sqrt{RaPr} \langle \nu T \rangle_{x,t} - \langle \partial_z T \rangle_{x,t}$  and the Reynolds number  $Re = \sqrt{Ra/Pr} \sqrt{\langle |\mathbf{u}|^2 \rangle_{V,t}}$ , measuring the global heat transfer efficiency and flow strength, respectively. Here,  $\langle \cdot \rangle_{x,t}$  denotes taking the average over a horizontal plane and time, and  $\langle \cdot \rangle_{V,t}$  denotes taking the average over the two-dimensional space and time. Note that we use the temperature gradients at the top and

bottom plates, i.e.,  $z = 0$  and  $z = 1$ , to obtain the  $Nu$  results, and this method has been verified in the previous work.<sup>35</sup>

To solve the momentum equations for fluid–solid interactions, we apply a direct-forcing immersed boundary method (IBM) in the Euler–Lagrange framework.<sup>36,37</sup> In each Runge–Kutta step, advancing the momentum equations in time without considering the IBM force  $\mathbf{f}$  gives a prediction velocity, which is interpolated to the Lagrangian grid using the moving-least squares approach.<sup>38,39</sup> The force  $\mathbf{f}$  is calculated using no-slip and no-penetration conditions on the surface of the particles, which is then spread back to the Eulerian grid to update the velocity and correct pressure distribution.

A volume of fluid (VoF) model is adopted to solve the energy equation of both phases, and a phase indicator,  $\zeta$ , is defined to quantify the volume fraction of the solid phase. To distinguish the solid and the fluid phase, a level-set function  $\zeta$  is defined such that  $\zeta < 0$  inside the solid obstacle and  $\zeta > 0$  outside the obstacle. The phase indicator  $\zeta$  can be determined using the following formula:<sup>40,41</sup>

$$\zeta = \frac{\sum_{n=1}^4 -\zeta_n \mathcal{H}(-\zeta_n)}{\sum_{n=1}^4 |\zeta_n|}, \quad (2)$$

where  $\zeta_n$  are for four corner nodes, and  $\mathcal{H}$  is the Heaviside step function. By using  $\zeta$ , the velocity of the combined phase  $\mathbf{u}_{cp}$  can be expressed as

$$\mathbf{u}_{cp} = \zeta \mathbf{u}_p + (1 - \zeta) \mathbf{u}_f, \quad (3)$$

where  $\mathbf{u}_f$  is the velocity in fluid, and  $\mathbf{u}_p$  is the velocity in solid obstacles, which satisfies  $\mathbf{u}_p = \mathbf{0}$  obviously for fixed obstacles.

We computed the dynamic and thermal effects of flow in porous media with two phases by coupling the IBM method with the VoF method. To discretize the governing equations, a uniform Cartesian grid is constructed, and the second-order central finite-difference method is applied. Time stepping is achieved by a fractional-step third-order Runge–Kutta scheme for the explicit terms and a Crank–Nicholson scheme for the implicit terms.<sup>42</sup> The grid resolution in this study is chosen to be  $1080 \times 1080$  in order to fully resolve both the boundary layers and the obstacles in the bulk area. For more details

including considerations of selecting grid resolutions, we refer the readers to our previous work by Liu *et al.*,<sup>32</sup> and for the numerical schemes of the governing equations in depth, we refer the reader to the constructive work by van der Poel *et al.*<sup>42</sup>

To investigate the effect of  $Pr$  on the heat transport process, we select the  $Pr$  number to be 0.03 and 0.1, as opposed to large  $Pr = 4.3$  and 10.  $Ra$  is fixed at  $10^8$  with reference to the parameters of the previous work,<sup>32</sup> where the porous media enhance the heat transfer at high  $Pr$  for a wide range of porosity, with the maximum around  $\phi = 0.82$ . The diameter of the obstacles remains constant at  $D = 0.04$ , but the distribution of the obstacles changes with  $N$  from 0 (traditional RB) to 14, covering porosity  $\phi$  from 1 to 0.75 accordingly. Through simulations over at least 1000 non-dimensional time units, the Nusselt and Reynolds numbers are obtained after the system reaches a statistically stationary state. To be more specific, the fluctuation level  $\eta_{Nu}$  is the relative difference of  $Nu$  based on the first and second halves of the simulations. Generally,  $\eta_{Nu} < 2\%$  is guaranteed, thus ensuring good statistical convergence.<sup>35</sup>

### III. RESULTS AND DISCUSSION

#### A. Heat transfer

As the most important response parameter in RB convection, the heat transfer efficiency  $Nu$  is examined in detail at first. In Fig. 2(a), the  $\phi$  dependence of  $Nu$  for different  $Pr$  values is shown. We can observe an enhancement of  $Nu$  and a similar trend of first increasing and then decreasing for different  $Pr$ . Note that the results of  $Pr = 4.3$  case are in agreement with the previous literature.<sup>32</sup>

If we normalize the  $Nu$  curves with respect to the traditional RB case, we can see more clearly the effect of  $Pr$  on the trend of heat transport. As shown in Fig. 2(b), within the parameter range studied, the normalized  $Nu(\phi)/Nu(1)$  curves exhibit two different trends: For large  $Pr = 4.3, 10$ ,  $Nu$  first increases and then decreases with decreasing  $\phi$ , and it is expected to be smaller than  $Nu(\phi = 1)$  when  $\phi$  is below 0.7 according to the previous work.<sup>32</sup> The optimal heat transport enhancement of 6.7% is observed when  $\phi = 0.82$  at  $Pr = 4.3$ . Meanwhile, for small  $Pr = 0.03, 0.1$ ,  $Nu$  also shows notable enhancement of around 6% with an advanced transition point and an earlier suppression. During the growth phase, the curves of the low  $Pr$  remain consistent with the curves of the high  $Pr$ ; however, the heat transfer at low  $Pr$  is suppressed earlier and more drastically.

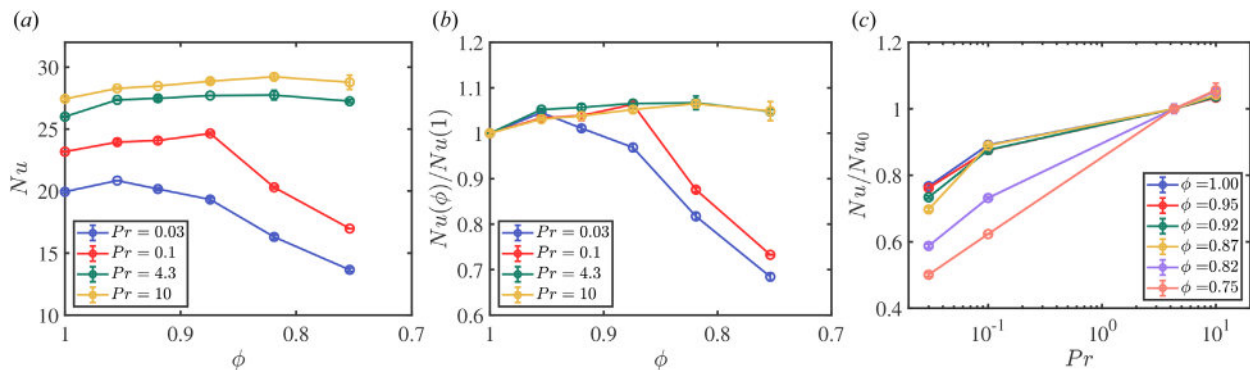


**FIG. 2.** (a) Variations of  $Nu$  with  $\phi$  for  $Pr = 0.03, 0.1, 4.3,$  and  $10$ . (b) Normalized  $Nu(\phi)/Nu(\phi = 1)$  with respect to traditional RB case for different  $Pr$ . (c) Semi-log plot of normalized  $Nu(Pr)/Nu_0$  for different porosities, where  $Nu_0$  is obtained at  $Pr = 4.3$ . The error bars represent statistical errors  $\eta_{Nu}$ .

We then plot normalized  $Nu$  vs  $Pr$  given a certain porosity, using  $Nu_0 = Nu(Pr = 4.3)$  as a baseline. As shown in Fig. 2(c),  $Nu$  shows an overall trend of increase with  $Pr$ . The  $Pr$  dependence of heat transport can be classified as two regimes as follows: For large  $Pr = 10$  cases,  $Nu$  curves under different porosity are closed to the traditional RB case and exhibit weak dependence on  $\phi$ ; however, for small  $Pr$ ,  $Nu$  curves of low porosity begin to deviate from others. For example, comparing the porosity of 0.87 and 0.75, the relative difference of  $Nu(\phi)/Nu_0$  is only 1.4% at  $Pr = 10$ , while the difference reaches 30% at  $Pr = 0.1$ . Since  $Nu$  varies widely under different porosity, indicating that in low- $Pr$  cases, the effect of porosity on the global heat transport is more significant. This is similar to the numerical research on confinement-induced RB convection, where the  $Pr$  dependence of  $Nu$  under different aspect ratios varies considerably. Here, the different trends can be classified as two regimes:  $Pr \leq 0.5$ , for which  $Nu$  increases with decreasing  $\Gamma$ , and  $Pr = 0.1, 0.2$ , for which no significant  $Nu$  enhancement is seen.<sup>23</sup> Such a classification according to high- and low- $Pr$  is in line with the trends we obtained, so it is of great importance to explore in detail the transition of our system subject to  $Pr$  variation.

In general, we find both similarities and differences in the heat transport trends for the low- and high- $Pr$  cases. In Liu's work at  $Pr = 4.3$ , the mechanism of this non-monotonic trend is explained as a combination of flow coherence enhancement and flow obstruction by viscosity.<sup>32</sup> As  $Pr$  decreases, the viscous effect decreases as well. According to this explanation, heat transfer should be less inhibited,

which is contrary to our findings. Therefore, at low  $Pr$ , it is probable that the new mechanism inhibits heat transfer. In order to figure it out, we will further analyze the flow structures, coherent structures, and boundary layers in Secs. III B–III D, attempting to investigate in detail the effect of  $Pr$  variation on RB convection in porous media.

### B. Flow structure

To explain why the porous media significantly impact heat transfer in the low- $Pr$  case, we further investigate the flow structures under different  $Pr$  values. Figure 3 shows the instantaneous snapshots of non-dimensional temperature, velocity magnitude, and local vertical heat flux fields at  $Pr = 0.1$  and  $Pr = 4.3$ , while  $\phi = 0.92$ . Note that the range scales of temperature and velocity magnitude fields are set to be different for  $Pr = 0.1$  and  $Pr = 4.3$ . The local vertical heat flux is defined as  $v \cdot \delta T$  at each point, where  $\delta T = T - T_m$  is the temperature fluctuation, with respect to the mean temperature  $T_m = 1/2$ ; given the  $Pr$  difference, we compensate the heat flux as  $\sqrt{RaPr} v \cdot \delta T$  to characterize heat transfer intensity better so that the integral of vertical heat flux along any horizontal plane gives the Nusselt number at that moment.

As we know, in the traditional 2D RB convection with  $\phi = 1$ , the typical flow structure consists of a well-organized large-scale circulation and two counter-rotating corner rolls. The LSC structure has also been found inside a cubic RB cell with a tendency to align along the diagonal planes.<sup>13</sup> In our case with porous structures at  $Pr = 0.1$ , as

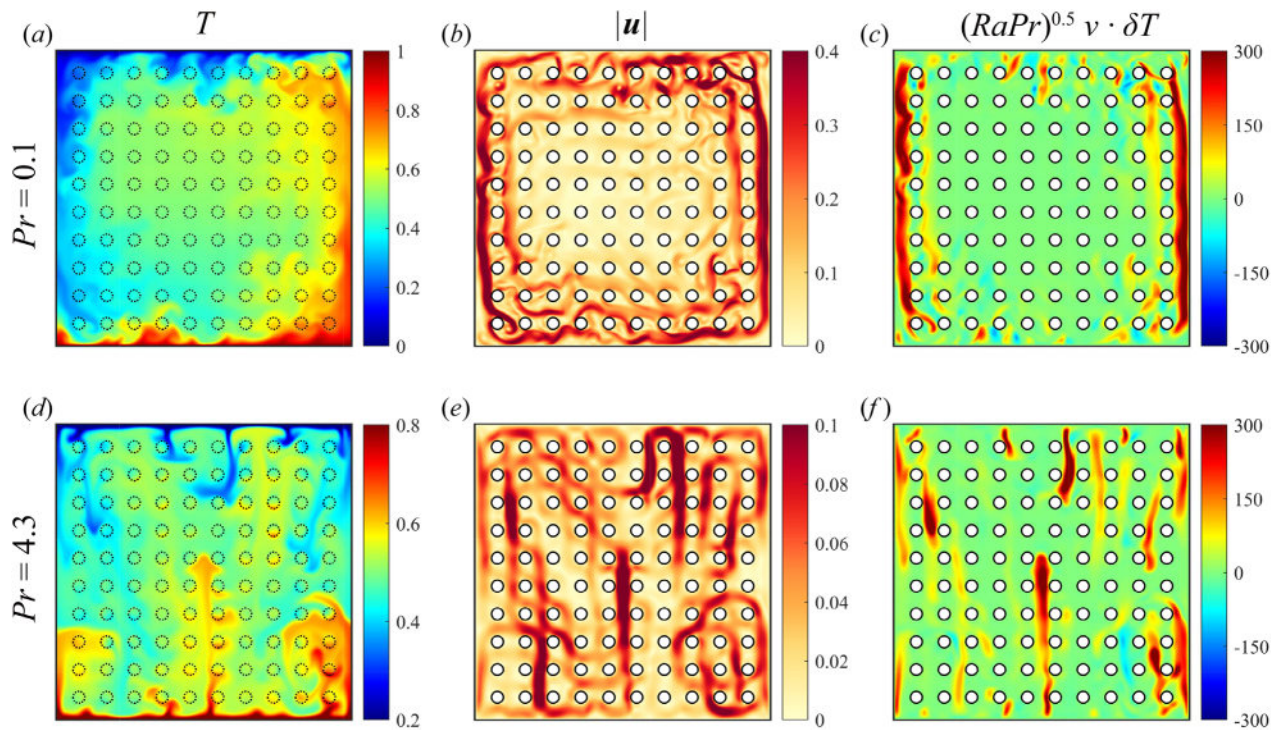


FIG. 3. Typical snapshots of the instantaneous temperature  $T$  in (a) and (d), the velocity magnitude  $|u|$  in (b) and (e) and the compensated vertical convective heat flux  $\sqrt{RaPr} v \cdot \delta T$  in (c) and (f) at  $Ra = 10^8$ ,  $\phi = 0.87$ ,  $Pr = 0.1$  for (a)–(c) and  $Pr = 4.3$  for (d)–(f). Dotted circles in (a) and (d) indicate that the temperature in the obstacles is well defined, while white circles in other subplots indicate that the velocity inside the obstacles is zero.

shown in Figs. 3(a) and 3(b), the temperature field snapshot exhibits a similar LSC structure with plumes near the sidewalls and a bulk of nearly no plume. Due to the geometric confinement of the obstacle array, the flow circulates through the convective channels in a regular way, and the velocity is close to zero in the center area. It can also be seen from Fig. 3(c) that the strong vertical heat flux mainly occurs in the channels near the two sidewalls.

At  $Pr = 4.3$ , from Fig. 3(d), we can see that the hot plumes are detached from the bottom boundary layer, rise through the flow channel in the bulk area, and mix with the downward cold plumes to transfer heat. Moreover, in Fig. 3(e), the flow strength is reduced significantly, with upward convective channels formed in the bulk area instead of the circulation structure. As opposed to local heat flux near sidewalls, the coherent structures are formed between the obstacles and distributed throughout the system, as illustrated in Fig. 3(f).

In the traditional RB convection, the effect of Prandtl number on the flow structures has been discussed.<sup>43,44</sup> At low  $Pr$ , it is reported that plume emission from the plate regions is likely to be inhibited due to large wind shear.<sup>44</sup> Therefore, the plumes move to the right, merge together subject to LSC, and move upward along the sidewall to finally reach the top plate. In high- $Pr$  cases, however, as the viscous effect increases, the large-scale flow strength reduces significantly; instead, the rising plumes play a more critical role.<sup>43</sup> Similarly, in our system, in the presence of the porous matrix, the difference between the flow structures at high and low  $Pr$  is more obvious; the increase in  $Pr$  also leads to the dominance of thermal plumes rather than large-scale circulation in terms of global heat transport.

We further examined the Reynolds number to characterize the convection strength of the flow field. The log-log plot in Fig. 4(a) shows a decreasing trend of  $Re$  for different  $Pr$  values with a scaling law close to  $Re \sim Pr^{-5/6}$  from the Grossman-Lohse (GL) theory for boundary layer dominated systems.<sup>1</sup> From the normalized  $Re(\phi)/Re(\phi = 1)$  for different  $Pr$  in Fig. 4(b), we can see that the flow strength reduces monotonically with decreasing porosity, which is caused by the increasing resistance exerted by obstacles. To be more specific, the inclusion of porous media (with respect to the traditional

RB) leads to more significant flow weakening compared to a further decrease in porosity. For instance, in the  $Pr = 0.1$  case, from  $\phi = 1$  to  $\phi = 0.95$ ,  $Re$  decreases by 67.4%; when the porosity further decreases from 0.95 to 0.75,  $Re$  only continues to decrease by 17.6% of  $Re$  of  $\phi = 1$ . Though the volume averaged flow strength decreases significantly, the heat transfer efficiency can even increase, which is consistent with previous findings that the slower flow might transfer more heat under certain stabilizing conditions.<sup>6</sup>

### C. Coherent structure

Manipulating coherent structures in turbulent flows is a newly discovered way to regulate heat transport properties.<sup>45</sup> In this study, the array of solid obstacles, namely, porous structures, serve as a geometric modification and a stabilizing effect, thus forming and affecting the coherent structures in the thermal convection system. In Fig. 5, we demonstrate the local coherence property by plotting the joint probability density functions (PDFs) on the middle horizontal plane  $z = 0.5$ , between the vertical velocity  $v$  and the temperature fluctuation  $\delta T$ . Moreover, to measure the flow coherence quantitatively, we consider the cross correlation  $C$  of  $v$  and  $\delta T$  and calculate its value as

$$C = \frac{\langle (v - \langle v \rangle_{x,t})(\delta T - \langle \delta T \rangle_{x,t}) \rangle_{x,t}}{\sqrt{\langle v^2 \rangle_{x,t} - \langle v \rangle_{x,t}^2} \sqrt{\langle \delta T^2 \rangle_{x,t} - \langle \delta T \rangle_{x,t}^2}} \quad (4)$$

The values of  $C = 1$  and  $C = -1$  correspond to perfect correlations and anti-correlations, respectively, and  $C = 0$  corresponds to no correlation.

As we can see in Fig. 5, the local temperature fluctuation and vertical velocity are generally distributed in the lower left and upper right regions, showing an overall positive correlation. This is because hot fluid tends to move upward due to buoyancy, and vice versa. Moreover, we can obtain more information about flow coherence by comparing the trends of PDFs and the cross correlation values. By comparing the upper and lower subplots under the same porosity, we can observe that for  $Pr = 0.1$  case, both the range of velocity

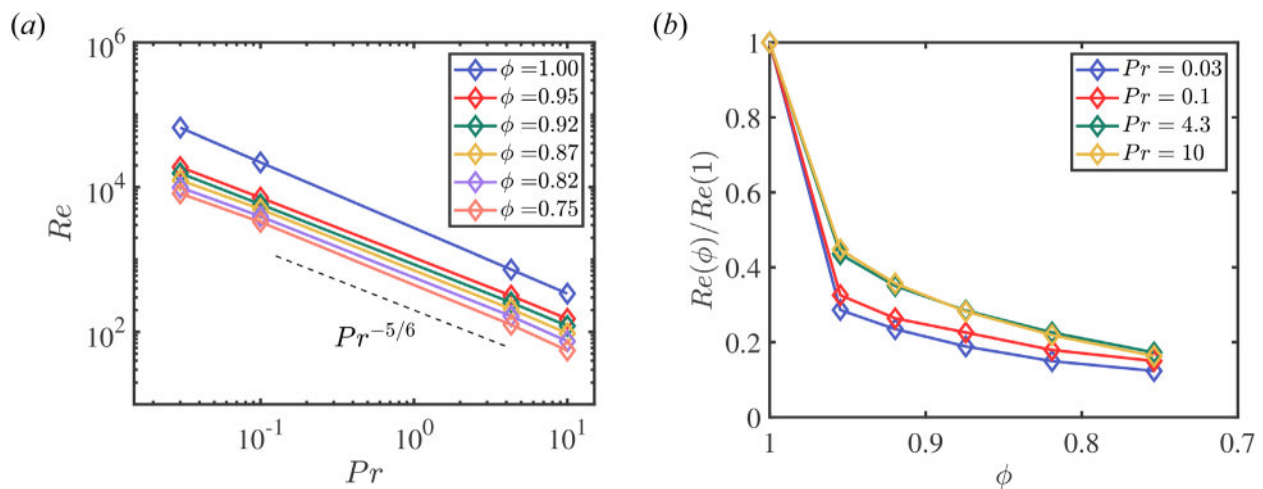


FIG. 4. (a) Log-log plot of  $Re(Pr)$  under different porosity  $\phi = 1, 0.92, 0.87, 0.82, 0.75$ . For reference, the dashed line represents the GL scaling law  $Re \sim Pr^{-5/6}$ . (b) Normalized  $Re(\phi)/Re(\phi = 1)$  with respect to traditional RB case at  $Pr = 0.03, 0.1, 4.3, \text{ and } 10$ .

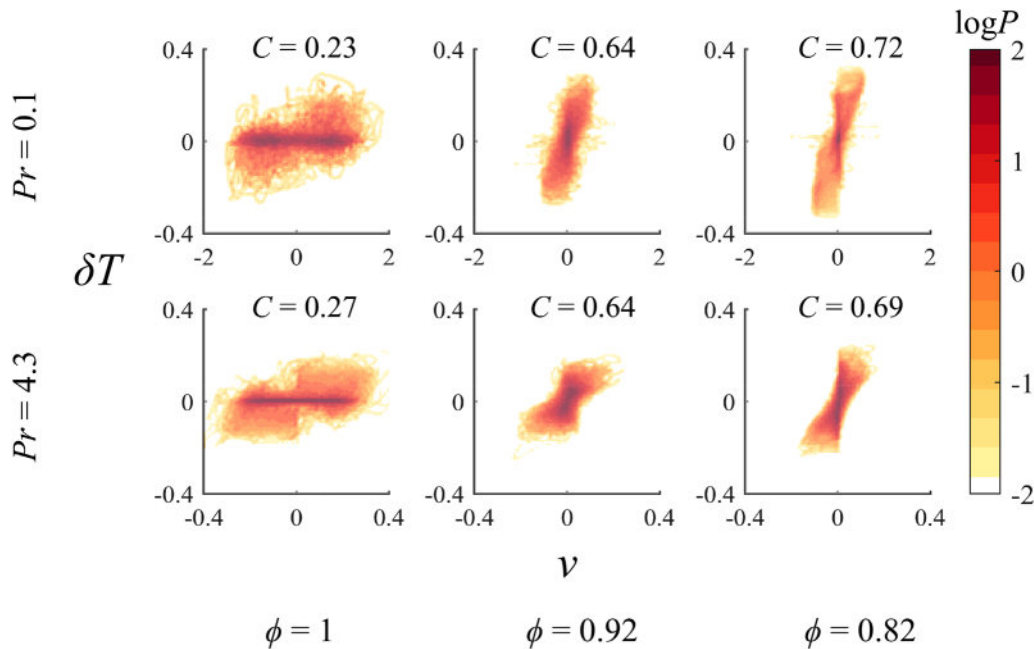


FIG. 5. The joint PDFs of the vertical velocity  $v$  and the temperature fluctuation  $\delta T$  on the horizontal plane  $z = 0.5$  at  $Pr = 0.1$  and  $4.3$ , under the porosity of  $\phi = 1, 0.92, 0.82$ . Corresponding values of the cross correlation  $C(v, \delta T)$  are labeled at the top of each subplot.

fluctuation and the temperature fluctuation level are much larger than those for the case of  $Pr = 4.3$ . Note that the horizontal axis scales of the two rows are set to be different. Considering the flow structure analysis in Sec. III B, we suggest that plumes in low- $Pr$  cases merge into the large-scale circulation and form an even stronger thermal plume structure near sidewalls, featuring a higher velocity and a more considerable temperature difference.

Additionally, by comparing three subplots along the row at the same  $Pr$ , it can be seen that with decreasing  $\phi$ , the velocity fluctuation exhibits a drastic reduction from the traditional RB case to porous RB case, which is caused by the obstruction from the obstacle array. Overall, as for the cross correlation coefficient between the vertical velocity and temperature, there is a leap between the traditional RB case ( $\phi = 1$ ) and the case with porous structures, and the correlation further increases gradually with decreasing  $\phi$ . The leap stage corresponds to the enhancement of  $Nu$ . This proves that increasing the number of obstacles (especially the inclusion of obstacles for the first time) can regulate the flow structure and increase the coherence of the flow and then enhance the heat transfer further.

However, the analysis of local bulk properties here cannot fully explain the trend of global heat transport. In general, we would assume a positive correlation between the heat transfer efficiency and flow coherence. As can be seen in Figs. 2(a) and 5, in the case of  $Pr = 0.1$ , we obtain  $Nu = 24.8$  and  $C(v, \delta T) = 0.64$  under  $\phi = 0.92$ , while  $Nu = 20.3$  and  $C(v, \delta T) = 0.72$  under  $\phi = 0.82$ , which shows an increase in coherence and yet a non-trivial reduction in the global heat transport. This counter-intuitive phenomenon can be further explained through the following analysis of the thermal boundary layer.

#### D. Thermal boundary layer

In our parameter space, the RB convection is dominated by the boundary layer, both for viscous dissipation and thermal dissipation. Therefore, the properties of the boundary layers are extremely important for the heat transfer of the system.<sup>1,5,46</sup> Here, to investigate the development of thermal boundary layer in detail, we use the slope method to give the thickness  $\delta_{th}(x)$  along the  $x$ -direction.<sup>46–48</sup> To be more specific, for every  $x = x_0$ ,  $\delta_{th}(x_0)$  is obtained from the slope of the time-averaged temperature profile  $\langle T(x_0, z) \rangle_t$  near the bottom plate and then locating the intersection point between the linear fitting line and minimum temperature  $\langle T_{min}(x_0) \rangle_t$  along the  $z$ -direction within  $z = 0$  to  $z = 1/2$ , namely, the bottom half of the cell. Due to the symmetry of the system, the boundary layer near the top plate behaves similarly; therefore, we only analyze the bottom thermal boundary layer.

Meanwhile, as for the viscous boundary layer, due to the presence of the obstacle array with the no-slip surface, the time-averaged velocity profile is close to a parabola through the bottom channel (gap between bottom plate  $z = 0$  and the bottom row of obstacles  $z = l$ ). In this situation, performing the slope method<sup>46</sup> or standard deviation method<sup>48</sup> to give the viscous boundary layer thickness is no longer practical. Thus, we mainly focus on the analysis of thermal boundary layer thickness in this section.

In Fig. 6, the thermal boundary layer thickness profiles  $\delta_{th}(x)$  at  $Pr = 0.1$  and  $4.3$  under different porosity are shown. For  $Pr = 0.1$  in Fig. 6(a), the boundary layer is flat in the middle and only slightly different near both sidewalls. When porosity decreases to  $0.82$ , we observe a sloping development of thermal boundary layer. The thermal boundary layer thickness  $\delta_{th}(x)$  increases with  $x$ , which shares similarity with the Prandtl–Blasius-type kinetic and thermal boundary

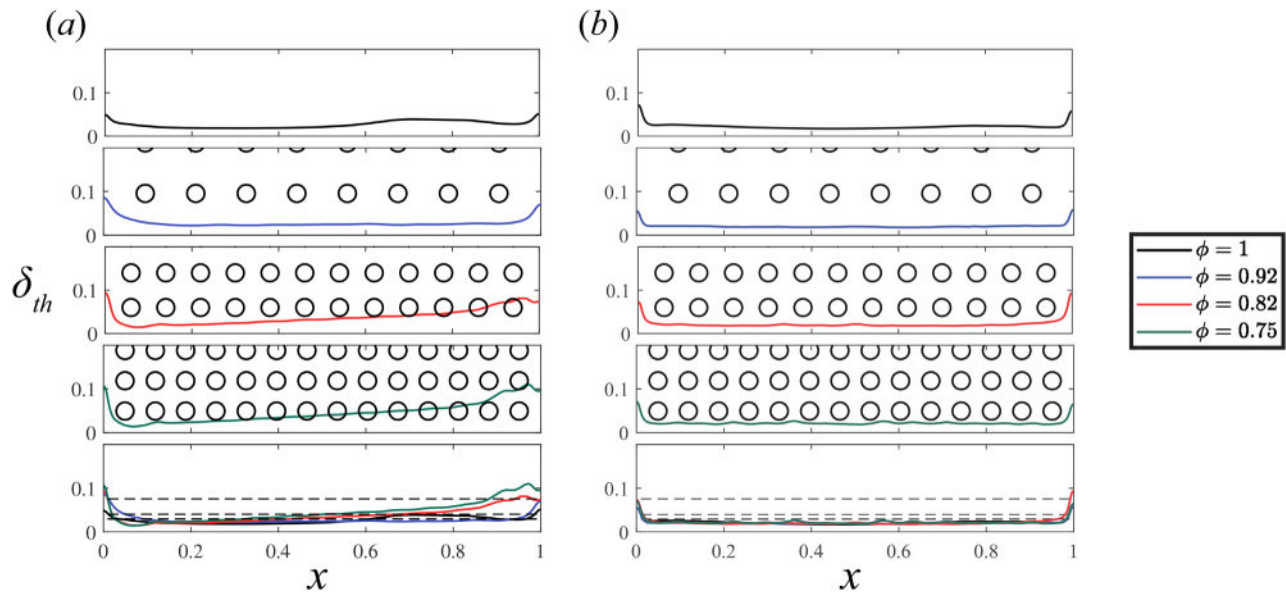


**FIG. 6.** Thermal boundary layer thickness profile  $\delta_{th}(x)$  under  $\phi = 1, 0.92, 0.82,$  and  $0.75$  at (a)  $Pr=0.1$  and (b)  $Pr=4.3$ . Circles represent the obstacle configuration in each subplot. Stacked plot of boundary layer profile under different porosities is shown in the bottom row, where the dashed lines represent the height of obstacles under different porosities.

layer as reported.<sup>49</sup> Furthermore, when the porosity decreases to 0.75, the upward-sloping trend becomes even more significant, which can be seen clearly in the stacked plot. When we overlap the boundary layers under different porosities, we find that on the left side, the boundary layer thickness is almost the same; with the fluid flowing to the right, the boundary layer thickens faster the smaller the porosity. This means that the heat transfer is suppressed mainly at the end of the wind shear. However, at  $Pr=4.3$ , the boundary layer thickness exhibits weak  $x$  dependence, and the boundary layer profiles are nearly the same for all porosity, flat in the middle and slightly warped near sidewalls, as shown in Fig. 6(b).

To further investigate the mechanism under boundary layer development, we now examine the snapshots of instantaneous temperature field  $T$  in the corresponding cases, as shown in Fig. 7. For  $Pr=4.3$  cases in Figs. 7(d)–7(f), we observe similar plume structures penetrating the porous media in the bulk region, as reported by Liu *et al.*<sup>32</sup> Under smaller porosity, as the resistance becomes greater and the turbulent mixing effect is weakened, the plumes further penetrate deep in the bulk area and form vertical convective channels through obstacles in Fig. 7(f).

From Figs. 7(a)–7(c) at low- $Pr$ , as porosity decreases, the temperature fluctuation in the bulk area becomes weaker. Moreover, unlike high- $Pr$  cases, the LSC structure persists under all porosity explored, and no convective channel through the bulk area is observed. This phenomenon is similar to previous findings that for confinement-induced RB systems, the LSC structure at low- $Pr$  is robust against the geometrical confinement, namely, different aspect ratios of the convection cell.<sup>23</sup> In Fig. 7(c), when  $\phi = 0.75$ , a regular LSC is observed with no apparent plume structures. In this case, all turbulent fluctuations disappear. A similar phenomenon is also found in partitioned RB convection systems, where many adiabatic boards are vertically inserted into the RB cell.<sup>22</sup>

Through the analysis of the thermal boundary layer, we can find that at low- $Pr$ , the strong horizontal wind shear in the bottom channel suppresses the emission of upward plumes and buries the heat within the LSC through the journey. Accordingly, more heat is stored, and the thermal boundary layer gets thicker with increasing  $x$ , as can be seen in Fig. 6(a). This also helps to explain the significant reduction in the global heat transport in Fig. 2(b), since the thicker thermal boundary layer has a smaller temperature gradient and thus inhibits heat transfer in the case of low porosity. Therefore, we speculate that the mechanism of heat transfer suppression at low- $Pr$  is different from the suppression at high- $Pr$ : It is because the strong LSC wind inhibits the plume from rising and mixing in the middle part; thus, a large amount of heat is carried to the right side, causing the boundary layer to thicken.

To further confirm our interpretation, we check the strength of the LSC and the turbulent fluctuations in the bottom channel at low- $Pr$ . We choose to examine the flow properties in the bottom channel, where  $0 < z < l$ , because the flow at low- $Pr$  is mainly concentrated in the peripheral region [see Fig. 3(b)]. As shown in Fig. 8, we plotted mean kinetic energy and the proportion of turbulent kinetic energy of the flow in the bottom channel. The mean kinetic energy  $E_k$  and the mean turbulent kinetic energy  $E'_k$  in the channel are defined as follows:

$$E_k = \frac{1}{2l} \left\langle \int_0^l |\mathbf{u}|^2 dz \right\rangle_t, \quad E'_k = \frac{1}{2l} \left\langle \int_0^l |\mathbf{u}'|^2 dz \right\rangle_t, \quad (5)$$

where  $\mathbf{u}' = \mathbf{u} - \langle \mathbf{u} \rangle_t$  is the velocity fluctuation at each point.

Although the global convection strength decreases monotonically with decreasing  $\phi$  [see Fig. 4(b)], we can see from Fig. 8(a) that there is no significant reduction in the kinetic energy in the bottom channel. For example, the mean kinetic energy of  $\phi = 0.75$  is generally larger than the kinetic energy of  $\phi = 0.82$ , which means that as the porosity



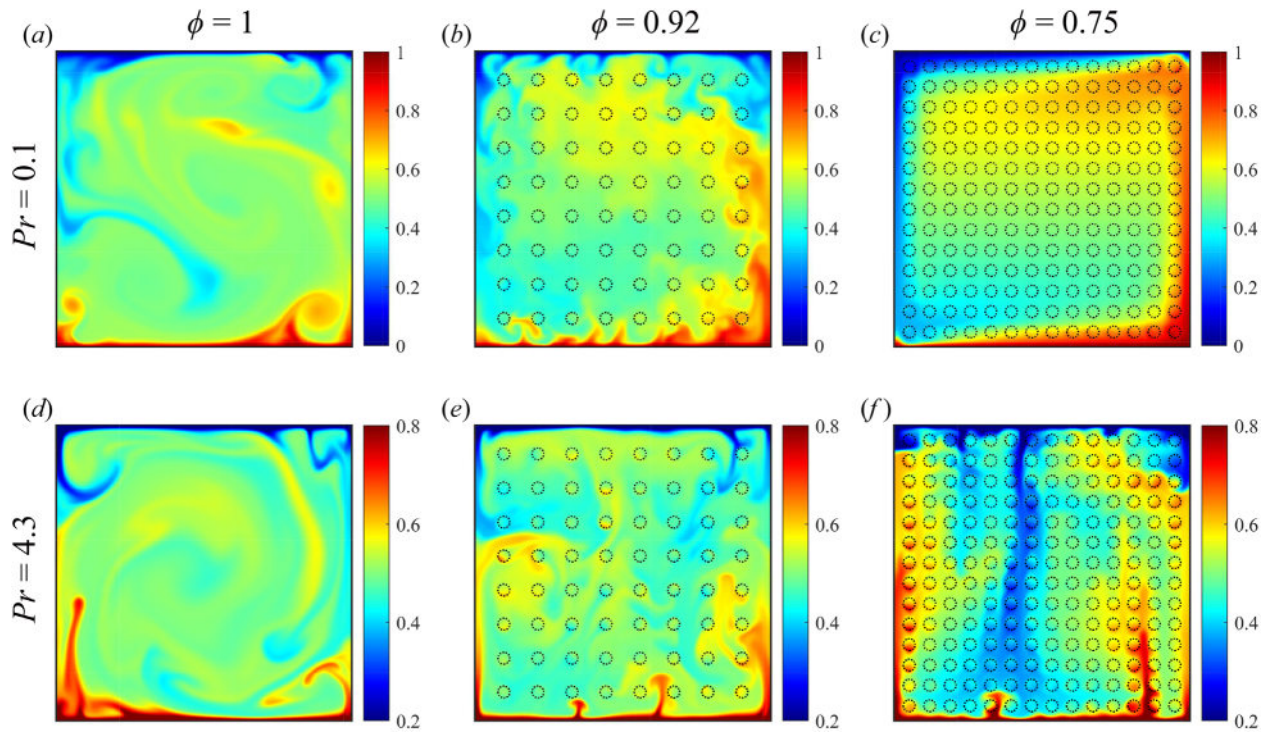


FIG. 7. Snapshots of the instantaneous temperature  $T$  under  $\phi = 1, 0.92,$  and  $0.75,$  at  $Pr = 0.1$  in (a)–(c) and  $Pr = 4.3$  in (d)–(f).

decreases, the wind strength can be even strengthened at low porosity. The stronger wind shear suppresses the plumes and heat transfer more. The curves of  $E_k$  exhibit fluctuations due to the inclusion of solid obstacles, and the fluctuations get more frequent under smaller porosity given more obstacles.

Given that the relative difference of mean kinetic energy is insignificant under different porosities, we can examine the proportion of

the turbulent kinetic energy on the mean kinetic energy to check the flow fluctuations. As shown in Fig. 8(b), the proportion of turbulent kinetic energy reduces with decreasing  $\phi$ , which means that the fluctuation strength decreases, the flow is stabilized gradually as the porosity decreases, and the flow channel becomes narrower. Once the porosity decreases to  $\phi = 0.75$ , the flow even becomes laminar. [Since the turbulent kinetic energy is all zero, this curve is not plotted in Fig. 8(b).]

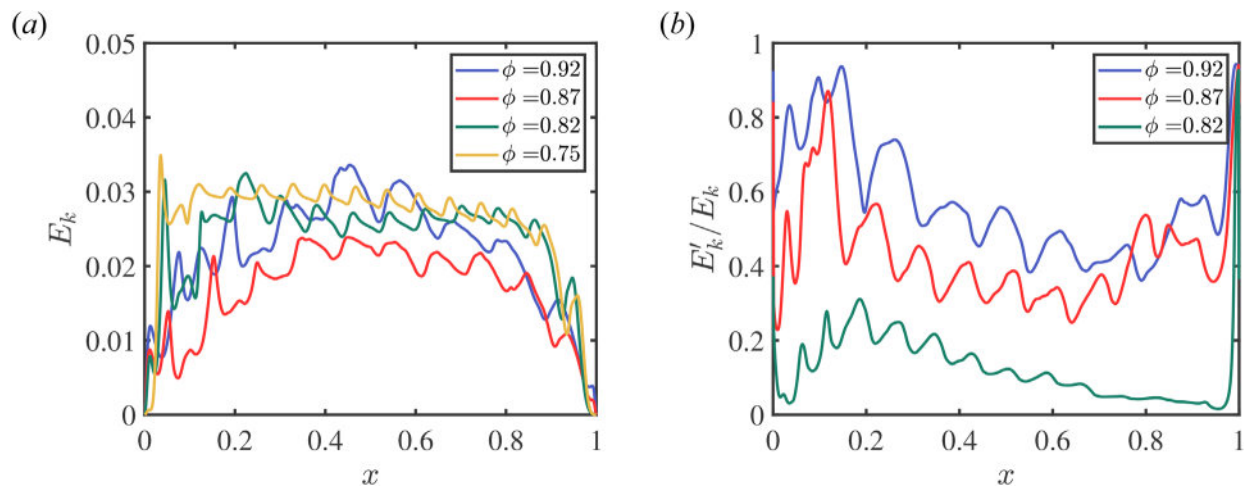


FIG. 8. (a) Mean kinetic energy in the bottom channel at  $Pr = 0.1$  under porosity  $\phi = 0.92, 0.87, 0.82,$  and  $0.75.$  (b) The ratio of turbulent kinetic energy to mean kinetic energy in the bottom channel at  $Pr = 0.1$  under porosity  $\phi = 0.92, 0.87,$  and  $0.82.$

Moreover, the turbulent kinetic energy decreases as fluid flows forward in the flow channel for each porosity, indicating that the turbulence becomes weaker along the flow direction. This reveals the stabilizing effect of the porous media on the flow at low  $Pr$ : not weakening the flow intensity, but weakening the flow fluctuations.

These findings confirm the hypothesis we made in our analysis of the thermal boundary layer. At high- $Pr$ , plumes rise at random time intervals and from random locations of the hot plate [see Figs. 7(d)–7(f)], and thus, the average over time gives a boundary layer profile with weak  $x$  dependence [see Fig. 6(b)]. Therefore, no sloping trend of boundary layer profile can be seen. However, in the low- $Pr$  cases under small porosity, at  $\phi \geq 0.82$ , strong LSC suppresses fluctuations and plume detachment, leading to the thickening boundary layer profile due to heat accumulation close to the end of the horizontal wind.

#### IV. RANDOM DISTRIBUTION

In the discussion above, we focused on the square lattice arrangement of obstacles as shown in Fig. 1. In this section, we further analyze how different obstacle arrangements influence the heat transport and flow structure and investigate the robustness of our results with respect to the obstacle configuration.

We construct the porous structures by randomly placing the circular obstacles with diameter  $D = 0.04L$  in the cell, with the condition that the minimum distance between any two obstacles or between any obstacle and the wall satisfies  $l_{min} \geq 0.01L$  for full resolution of pore scale.<sup>32</sup> The number of obstacles is selected to be the same as the corresponding regular obstacle arrays. The simulations are also performed at  $Pr = 0.1$  and 4.3.

In Fig. 9(a), the  $\phi$  dependence of normalized  $Nu$  at low- and high- $Pr$  is shown. The results of the cases with the square lattice distribution are shown in dashed lines for reference. A similar non-monotonic trend is observed at  $Pr = 4.3$ , with an enhancement of 4.8% relative to the traditional RB case, which is close to results with the square lattice distribution. However,  $Nu$  enhancement is absent at  $Pr = 0.1$  in random distribution cases for large porosity. Meanwhile,

under random distribution of obstacles, heat transfer is suppressed more drastically, both for high- $Pr$  and low- $Pr$ . The reason behind this may be the irregularity of the channel formed by the randomly distributed obstacles that both rising plumes and LSC are impeded. As for the flow strength, in Fig. 9(b), we observe consistent trends, where  $Re$  reduces monotonically with decreasing  $\phi$ . Also, resembling Fig. 4(a), the incorporation of a few porous structures leads to a drastic decrease in the flow strength.

The flow structure is also investigated in detail for random obstacle distribution cases. Figure 10 shows the instantaneous snapshots of temperature and the velocity magnitude at  $Pr = 0.1$  under different porosities. From Figs. 9(a) and 9(d), we can still see a typical LSC structure similar to Fig. 7(b). As the porosity decreases, due to the impedance from randomly distributed obstacles, the LSC may not stick near the bottom plate when it sweeps horizontally, and densely distributed obstacles can cause diversion and form a more irregular LSC, as illustrated in Figs. 10(b) and 10(c). Due to the limitations of this randomly distributed geometry, it may be difficult for the LSC to flow through the corner [like the lower right corner in Fig. 10(e)], which leads to a thickening of the thermal boundary layer here and further decreases the heat transfer efficiency. This may also be the reason why the randomly distributed heat transfer is more strongly suppressed at low- $Pr$ , as the large-scale circulation is partially detached from the bottom plate.

Furthermore, as the porosity decreases to 0.75, the thermal boundary layer profile in Fig. 10(c) is similar to that in Fig. 7(c) under the same porosity, though the flow is not laminar. We can see that the horizontal wind shear sweeps across the bottom plate and passes through several randomly located obstacles, generating multiple wake flows and exchanging heat with obstacles, which may have a non-trivial local effect on the thermal boundary layer development. Although the random distribution of obstacles has an effect on the boundary layer, since the strong LSC still exists, the overall flow structures are still similar to the regular distribution of obstacles.

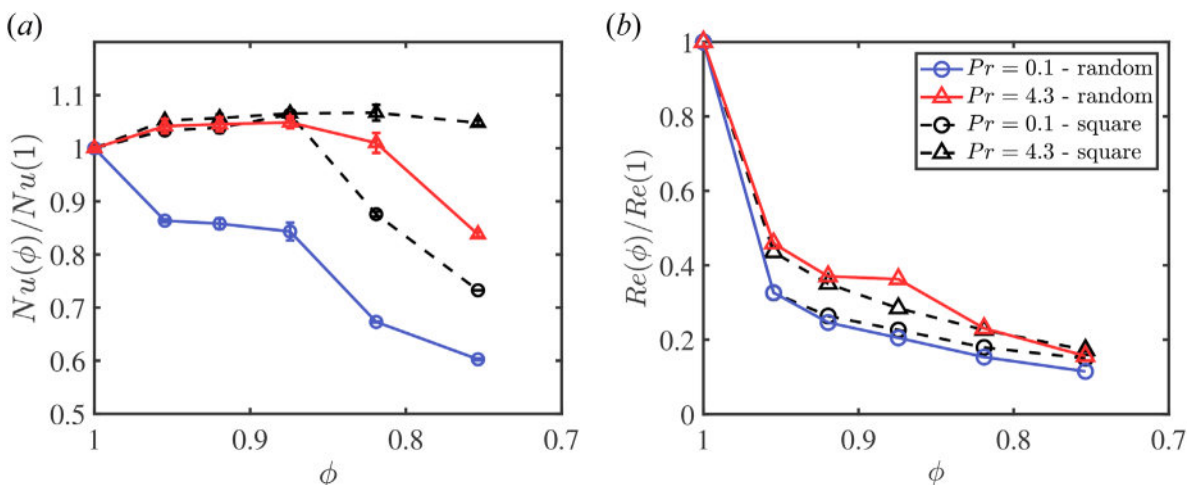
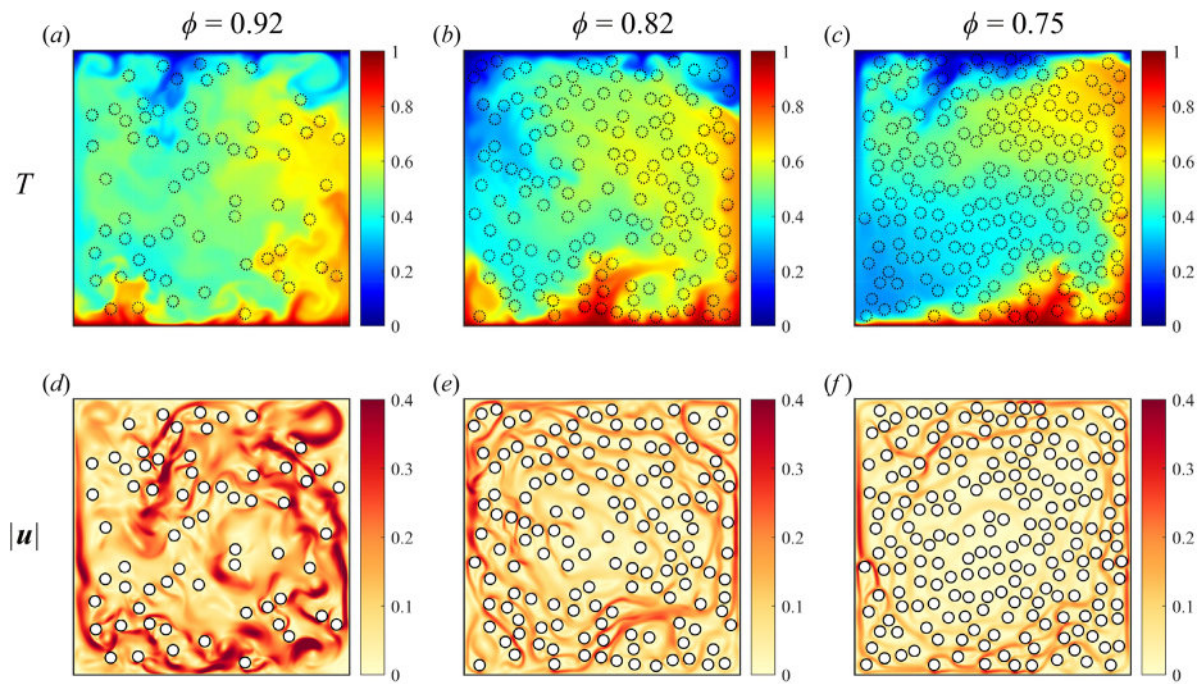


FIG. 9. Normalized  $Nu(\phi)/Nu(\phi = 1)$  in (a) and  $Re(\phi)/Re(\phi = 1)$  in (b) with respect to traditional RB case at  $Pr = 0.1$  and 4.3 with random distribution of obstacles. Dashed lines show the case with square lattice distribution for reference. Note that legends are shown in subplot (b). The error bars in the figure represent statistical errors  $\eta_{Nu}$ .



**FIG. 10.** Snapshots of the instantaneous temperature  $T$  in (a)–(c) and the velocity magnitude  $|\mathbf{u}|$  in (d)–(f) at  $Pr = 0.1$  under  $\phi = 0.92, 0.82$ , and  $0.75$ . Dotted circles in the temperature field and white circles in the velocity field indicate the randomly placed obstacles.

For  $Pr = 4.3$  case, our simulation results are consistent with previous findings<sup>32</sup> that the plume motion through the random distribution of obstacles is less organized than those in the square lattice distribution. The curved convection channels are formed instead of straight ones in order to adapt to randomly placed obstacles, leading to a slight reduction in the heat transport efficiency. As a comparison, the LSC structure in low- $Pr$  convection is significantly impeded and fragmented by the inclusion of obstacles, leading to a considerable reduction in  $Nu$ . This may contribute to explaining the absence of  $Nu$  enhancement in Fig. 9(a), as well as to confirm our findings that the robustness of LSC at low  $Pr$  and its dominance in heat transport.

## V. CONCLUSION

We have studied the heat transport and flow structure in low- $Pr$  porous-media RB convection using two-dimensional direct numerical simulations with the porous structures modeled by a set of no-slip circular solid obstacles located on a square lattice. Through the analysis of  $Nu$  vs  $\phi$  at different  $Pr$ , we find that at low  $Pr$  numbers, the global heat transport behaves non-monotonically as the number of obstacles increases, which is consistent with previous observations of non-monotonic  $Nu$  under different stabilization effects at high  $Pr$  number.<sup>6,32</sup> However, we surprisingly observe earlier suppression of  $Nu$  enhancement under large porosity, indicating that the effect of porosity on the global heat transport is more significant in low- $Pr$  cases. Different heat transport properties at low- and high- $Pr$  are also found in numerical research regarding RB convection under geometrical confinement.

To investigate the mechanism behind this, we perform further in-depth analysis. Through the instantaneous temperature, velocity

magnitude, and local heat flux snapshots, we figure out that the LSC structure is dominant in the global heat transport at low  $Pr$ . As a comparison, the dominance of thermal plumes and convective channels through bulk is reported at high  $Pr$ .<sup>32</sup> Furthermore, by the joint probability density functions between vertical velocity  $v$  and the temperature fluctuation  $\delta T$  on the middle horizontal plane, we find that porous matrix can regulate the flow structure and increase the flow coherence indeed, with a similar enhancement to the cross correlation coefficient for low  $Pr$  and high  $Pr$ . This means that the ability of porous media to increase coherence has more to do with the modification of geometry of the system than with viscous effects. The interval of the rapid increase in cross correlation coefficient coincides with the interval of heat transfer enhancement, indicating that the heat transfer enhancement at high and low  $Pr$  numbers has the same mechanism.

Furthermore, we investigate the thermal boundary layer at low  $Pr$  and observe an upward-sloping profile  $\delta_{th}(x)$  under low porosity. It is found that the emission of upward plumes is suppressed by the strong horizontal wind shear. For the bottom channel where there is flow shearing the thermal boundary layer, the flow strength is even strengthened as the porosity decreases. Meanwhile, the velocity fluctuations are suppressed not only with the fluid flowing forward but also with the porosity decreasing. This reveals the stabilizing effect of the porous media on the flow at low  $Pr$ : not weakening the flow intensity, but weakening the flow fluctuations.

Therefore, we believe that the dominant effects of porous media on the RB convection are different at low  $Pr$  and high  $Pr$ . At low  $Pr$ , the non-monotonic behavior of  $Nu(\phi)$  is mainly subject to two competing effects: The increase in flow coherence in the presence of porous media enhances heat transport, while strong horizontal wind-shear

and flow laminarization both contribute to the thickening of thermal boundary layer. By contrast, at high- $Pr$ , the non-monotonic trend of  $Nu$  is subject to two competing effects of enhanced flow coherence and increasing resistance as porosity decreases.

We also analyze how different obstacle arrangements influence the flow structure. Similar trends of global transport properties are obtained except for the absence of heat transport enhancement at low  $Pr$ . This is because the random distribution of obstacles makes the flow less organized and reduces the coherence of the flow. More importantly, we further confirmed that the flow structures in porous media are robust to different obstacle distributions: At low  $Pr$ , the LSC dominates the global heat transport, while at high  $Pr$ , the thermal plumes dominate. At low  $Pr$ , the LSC is still dominated but difficult to completely shear the boundary layer, which is the reason for the significant decrease in heat transfer.

In this study, we mainly focus on the effect of  $Pr$  on RB convection in porous media and observe a similar trend of heat transport with a different mechanism, which may provide valuable insight for some industrial scenarios, such as the design of heat exchangers, geothermal energy utilization, and CO<sub>2</sub> sequestration.<sup>30</sup> Our future work may extend the parameter space of the system and construct a 3D case to bring out even richer phenomena. Also, it will be of interest to investigate thermal convection systems with different stabilizing effects, such as wall shear, rotation, or vibration. Through this, we expect to obtain a more comprehensive understanding of  $Pr$  dependence in turbulent flows. Moreover, we intend to conduct experiments to compare with numerical simulation results, providing implications for both fundamental research and industrial design regarding thermal convection systems.

## ACKNOWLEDGMENTS

This work was financially supported by the National Natural Science Foundation of China under Grant No. 11988102 and the New Cornerstone Science Foundation through the XPLOER PRIZE.

## AUTHOR DECLARATIONS

### Conflict of Interest

The authors have no conflicts to disclose.

### Author Contributions

**Xuehao Zang:** Conceptualization (equal); Data curation (lead); Formal analysis (lead); Investigation (lead); Methodology (equal); Validation (equal); Visualization (lead); Writing – original draft (lead); Writing – review & editing (equal). **Jun Zhong:** Conceptualization (lead); Formal analysis (equal); Investigation (lead); Methodology (lead); Software (lead); Validation (lead); Visualization (equal); Writing – review & editing (lead). **Chao Sun:** Conceptualization (lead); Funding acquisition (lead); Investigation (equal); Project administration (lead); Resources (lead); Software (equal); Supervision (lead); Writing – review & editing (lead).

## DATA AVAILABILITY

The data that support the findings of this study are available from the corresponding author upon request.

## REFERENCES

- 1S. Grossmann and D. Lohse, "Scaling in thermal convection: A unifying theory," *J. Fluid Mech.* **407**, 27–56 (2000).
- 2B. I. Shraiman and E. D. Siggia, "Heat transport in high-Rayleigh-number convection," *Phys. Rev. A* **42**, 3650–3653 (1990).
- 3M. Karimzadeh, M. Khatibi, and S. N. Ashrafizadeh, "Impacts of the temperature-dependent properties on ion transport behavior in soft nanochannels," *Int. J. Heat Mass Transfer* **129**, 105728 (2021).
- 4M. Karimzadeh, M. Khatibi, S. N. Ashrafizadeh, and P. K. Mondal, "Blue energy generation by the temperature-dependent properties in funnel-shaped soft nanochannels," *Phys. Chem. Chem. Phys.* **24**, 20303–20317 (2022).
- 5G. Ahlers, S. Grossmann, and D. Lohse, "Heat transfer and large scale dynamics in turbulent Rayleigh-Bénard convection," *Rev. Mod. Phys.* **81**, 503–537 (2009).
- 6K. L. Chong, Y. Yang, S.-D. Huang, J.-Q. Zhong, R. J. A. M. Stevens, R. Verzicco, D. Lohse, and K.-Q. Xia, "Confined Rayleigh-Bénard, rotating Rayleigh-Bénard, and double diffusive convection: A unifying view on turbulent transport enhancement through coherent structure manipulation," *Phys. Rev. Lett.* **119**, 064501 (2017).
- 7Y. Yang, R. Verzicco, D. Lohse, and R. J. A. M. Stevens, "What rotation rate maximizes heat transport in rotating Rayleigh-Bénard convection with Prandtl number larger than one?," *Phys. Rev. Fluids* **5**, 053501 (2020).
- 8X. Zhu and Q. Zhou, "Flow structures of turbulent Rayleigh-Bénard convection in annular cells with aspect ratio one and larger," *Acta Mech. Sin.* **37**, 1291–1298 (2021).
- 9A. Xu, B.-R. Xu, L.-S. Jiang, and H.-D. Xi, "Production and transport of vorticity in two-dimensional Rayleigh-Bénard convection cell," *Phys. Fluids* **34**, 013609 (2022).
- 10D. Wang, J. Liu, Q. Zhou, and C. Sun, "Statistics of temperature and velocity fluctuations in supergravitational convective turbulence," *Acta Mech. Sin.* **39**, 122387 (2023).
- 11K.-Q. Xia, "Current trends and future directions in turbulent thermal convection," *Theor. Appl. Mech. Lett.* **3**, 052001 (2013).
- 12P. Wei, "The persistence of large-scale circulation in Rayleigh-Bénard convection," *J. Fluid Mech.* **924**, A28 (2021).
- 13V. T. Vishnu, A. K. De, and P. K. Mishra, "Dynamics of large-scale circulation and energy transfer mechanism in turbulent Rayleigh-Bénard convection in a cubic cell," *Phys. Fluids* **32**, 095115 (2020).
- 14G. Orian, A. Asulin, E. Tkachenko, N. Kleorin, A. Levy, and I. Rogachevskii, "Large-scale circulations in a shear-free convective turbulence: Mean-field simulations," *Phys. Fluids* **34**, 105121 (2022).
- 15B. Castaing, G. Gunaratne, F. Heslot, L. Kadanoff, A. Libchaber, S. Thomae, X.-Z. Wu, S. Zaleski, and G. Zanetti, "Scaling of hard thermal turbulence in Rayleigh-Bénard convection," *J. Fluid Mech.* **204**, 1–30 (1989).
- 16H. Jiang, D. Wang, S. Liu, and C. Sun, "Experimental evidence for the existence of the ultimate regime in rapidly rotating turbulent thermal convection," *Phys. Rev. Lett.* **129**, 204502 (2022).
- 17S. Bhattacharya, M. K. Verma, and A. Bhattacharya, "Predictions of Reynolds and Nusselt numbers in turbulent convection using machine-learning models," *Phys. Fluids* **34**, 025102 (2022).
- 18A. Blass, X. Zhu, R. Verzicco, D. Lohse, and R. J. A. M. Stevens, "Flow organization and heat transfer in turbulent wall sheared thermal convection," *J. Fluid Mech.* **897**, A22 (2020).
- 19D. Goluskin, H. Johnston, G. R. Flierl, and E. A. Spiegel, "Convectively driven shear and decreased heat flux," *J. Fluid Mech.* **759**, 360–385 (2014).
- 20X. Zhu, R. J. A. M. Stevens, O. Shishkina, R. Verzicco, and D. Lohse, "Scaling enabled by multiscale wall roughness in Rayleigh-Bénard turbulence," *J. Fluid Mech.* **869**, R4 (2019).
- 21C. Wang, L.-F. Jiang, H.-C. Jiang, C. Sun, and S. Liu, "Heat transfer and flow structure of two-dimensional thermal convection over ratchet surfaces," *J. Hydrodyn.* **33**, 970–978 (2021).
- 22J. Chen, Y. Bao, Z. X. Yin, and Z. S. She, "Theoretical and numerical study of enhanced heat transfer in partitioned thermal convection," *Int. J. Heat Mass Transfer* **115**, 556–569 (2017).
- 23K. L. Chong, S. Wagner, M. Kaczorowski, O. Shishkina, and K.-Q. Xia, "Effect of Prandtl number on heat transport enhancement in Rayleigh-Bénard convection under geometrical confinement," *Phys. Rev. Fluids* **3**, 013501 (2018).

- <sup>24</sup>B.-F. Wang, Q. Zhou, and C. Sun, "Vibration-induced boundary-layer destabilization achieves massive heat-transport enhancement," *Sci. Adv.* **6**, eaaz8239 (2020).
- <sup>25</sup>M. R. Soltanian, M. A. Amooie, Z. Dai, D. Cole, and J. Moortgat, "Critical dynamics of gravito-convective mixing in geological carbon sequestration," *Sci. Rep.* **6**, 35921 (2016).
- <sup>26</sup>X. Fu, L. Cueto-Felgueroso, D. Bolster, and R. Juanes, "Rock dissolution patterns and geochemical shutdown of CO<sub>2</sub>-brine-carbonate reactions during convective mixing in porous media," *J. Fluid Mech.* **764**, 296–315 (2015).
- <sup>27</sup>Y. Cinar and A. Riaz, "Carbon dioxide sequestration in saline formations. II. Review of multiphase flow modeling," *J. Pet. Sci. Eng.* **124**, 381–398 (2014).
- <sup>28</sup>D. A. Nield and A. Bejan, "Heat transfer through a porous medium," in *Convection in Porous Media* (Springer, 2017), pp. 37–55.
- <sup>29</sup>I. Ataei-Dadavi, M. Chakkingal, S. Kenjeres, C. R. Kleijn, and M. J. Tummers, "Flow and heat transfer measurements in natural convection in coarse-grained porous media," *Int. J. Heat Mass Transfer* **130**, 575–584 (2019).
- <sup>30</sup>D. R. Hewitt, "Vigorous convection in porous media," *Proc. R. Soc. A* **476**, 20200111 (2020).
- <sup>31</sup>T. Le Reun and D. R. Hewitt, "High-Rayleigh-number convection in porous fluid layers," *J. Fluid Mech.* **920**, A35 (2021).
- <sup>32</sup>S. Liu, L. Jiang, K. L. Chong, X. Zhu, Z.-H. Wan, R. Verzicco, R. J. Stevens, D. Lohse, and C. Sun, "From Rayleigh-Bénard convection to porous-media convection: How porosity affects heat transfer and flow structure," *J. Fluid Mech.* **895**, A18 (2020).
- <sup>33</sup>"Fluids," in *Microfluidics: Modelling, Mechanics and Mathematics*, edited by B. E. Rapp (Elsevier, 2017), Chap. 9, pp. 243–263.
- <sup>34</sup>J. Zhong, S. Liu, and C. Sun, "On the thermal effect of porous material in porous media Rayleigh-Bénard convection," *Flow* **3**, E13 (2023).
- <sup>35</sup>J. A. M. Stevens, R. Verzicco, and D. Lohse, "Radial boundary layer structure and Nusselt number in Rayleigh-Bénard convection," *J. Fluid Mech.* **643**, 495–507 (2010).
- <sup>36</sup>M. Uhlmann, "An immersed boundary method with direct forcing for the simulation of particulate flows," *J. Comput. Phys.* **209**, 448–476 (2005).
- <sup>37</sup>W.-P. Breugem, "A second-order accurate immersed boundary method for fully resolved simulations of particle-laden flows," *J. Comput. Phys.* **231**, 4469–4498 (2012).
- <sup>38</sup>M. Vanella and E. Balaras, "A moving-least-squares reconstruction for embedded-boundary formulations," *J. Comput. Phys.* **228**, 6617–6628 (2009).
- <sup>39</sup>M. D. de Tullio and G. Pascazio, "A moving-least-squares immersed boundary method for simulating the fluid-structure interaction of elastic bodies with arbitrary thickness," *J. Comput. Phys.* **325**, 201–225 (2016).
- <sup>40</sup>M. N. Ardekani, O. Abouali, F. Picano, and L. Brandt, "Heat transfer in laminar Couette flow laden with rigid spherical particles," *J. Fluid Mech.* **834**, 308–334 (2018).
- <sup>41</sup>T. Kempe and J. Fröhlich, "An improved immersed boundary method with direct forcing for the simulation of particle laden flows," *J. Comput. Phys.* **231**, 3663–3684 (2012).
- <sup>42</sup>E. P. van der Poel, R. Ostilla-Mónico, J. Donners, and R. Verzicco, "A pencil distributed finite difference code for strongly turbulent wall-bounded flows," *Comput. Fluids* **116**, 10–16 (2015).
- <sup>43</sup>B. A. Puthenveetil and J. H. Arakeri, "Plume structure in high-Rayleigh-number convection," *J. Fluid Mech.* **542**, 217 (2005).
- <sup>44</sup>E. P. Van Der Poel, R. Verzicco, S. Grossmann, and D. Lohse, "Plume emission statistics in turbulent Rayleigh-Bénard convection," *J. Fluid Mech.* **772**, 5–15 (2015).
- <sup>45</sup>K.-Q. Xia, S.-D. Huang, Y.-C. Xie, and L. Zhang, "Tuning heat transport via coherent structure manipulation: Recent advances in thermal turbulence," *Nat. Sci. Rev.* nwad012 (to be published).
- <sup>46</sup>Q. Zhou and K.-Q. Xia, "Measured instantaneous viscous boundary layer in turbulent Rayleigh-Bénard convection," *Phys. Rev. Lett.* **104**, 104301 (2010).
- <sup>47</sup>J. D. Scheel, E. Kim, and K. R. White, "Thermal and viscous boundary layers in turbulent Rayleigh-Bénard convection," *J. Fluid Mech.* **711**, 281–305 (2012).
- <sup>48</sup>Q. Zhou and K.-Q. Xia, "Thermal boundary layer structure in turbulent Rayleigh-Bénard convection in a rectangular cell," *J. Fluid Mech.* **721**, 199–224 (2013).
- <sup>49</sup>O. Shishkina, R. J. A. M. Stevens, S. Grossmann, and D. Lohse, "Boundary layer structure in turbulent thermal convection and its consequences for the required numerical resolution," *New J. Phys.* **12**, 075022 (2010).